Dalton Transactions

ROYAL SOCIETY OF CHEMISTRY

PAPER

View Article Online
View Journal | View Issue

Open Access Article. Published on 07 November 2025. Downloaded on 1/31/2026 4:42:54 PM.
This article is licensed under a Creative Commons Attribution-NonCommercial 3.0 Unported Licence.

Check for updates

Cite this: *Dalton Trans.*, 2025, **54**, 17991

Syntheses, crystal structures, and proton conduction properties of two zirconium fluorophosphonates

Shuzhen Liu,[a,b,c] Yingying Zhao,[b,c] Yuwei Ren,[a,b,c] Ziyuan Chen,[b,c,d] Lu Yang,[b,e] Zhihua Chen,[b,e] Zhongxin Wei,[d] Haiyan Sun, *[b,e] Meiling Feng *[b,e] and Xiaoying Huang [b,e]

By introducing hydrogen fluoride (HF) and a competitive ligand into the synthetic system to enhance the crystallinity of products, two two-dimensional (2D) zirconium fluorophosphonate compounds with high crystallinity, namely $A_2[Zr(hedp)F_2]$ ($hedpH_2$ = 1-hydroxyethylidene-1,1-diphosphonic acid, $A^+ = K^+$ (**1**), NH_4^+ (**2**)), were successfully prepared. Their structures feature the anionic layer of $[Zr(hedp)F_2]_n^{2n-}$ with A^+ cations located in interlayer spaces. The unique coexistence of F, −OH, and $-PO_3$ moieties within the structure generates an extensive hydrogen-bonding network, facilitating efficient proton transport. At the temperature of 85 °C and the relative humidity (RH) of 95%, the proton conductivity (σ) of compounds **1** and **2** is 6.37×10^{-4} S cm^{-1} and 1.27×10^{-2} S cm^{-1}, respectively. The proton conductivities of both compounds follow the Grotthuss mechanism. Compound **2** demonstrates better proton conductivity owing to the presence of NH_4^+ cations, which facilitate the formation of extensive hydrogen-bonding networks that enable efficient proton transport. This study endows the zirconium fluorophosphate family with new members and provides a feasible research strategy for constructing highly crystalline metal fluorophosphonate compounds.

Received 1st August 2025,
Accepted 3rd November 2025

DOI: 10.1039/d5dt01846c

rsc.li/dalton

Introduction

Due to their remarkable stability and adjustable pore architectures, zirconium-based metal–organic frameworks (Zr-MOFs) have shown promising potential in diverse applications including gas adsorption[1] and separation,[2] proton conduction,[3] and catalysis. However, the development of Zr-MOFs has always been hindered by their poor crystallinity.[4] The reason is that the high charge density of Zr^{4+} ions induces rapid nucleation and high sensitivity of the crystallization process to reaction conditions such as temperature, solvent, and ligand concentration.[5] Consequently, despite their excellent properties, it remains challenging to form high-quality crystals for Zr-MOFs. This limitation results in a restricted diversity of structural types and hinders in-depth mechanistic investigations for Zr-MOFs.

To date, the structural diversity of reported Zr-MOFs remains limited, being classified into major categories based on their ligands including zirconium carboxylates,[6] zirconium phosphates,[7] zirconium phosphonates,[8] nitrogen-containing heterocycle-based Zr-MOFs,[9] and macrocycle/porphyrin-based[10] Zr-MOFs. Among these, zirconium phosphonates exhibit superior chemical, mechanical, and thermal stability, as well as enhanced hydrolytic resistance compared to zirconium carboxylates and other Zr-MOFs.[11,12] The crystallization of zirconium phosphonates is generally more intricate, as their low crystallinity poses substantial difficulties for structural characterization.[13] For example, the structures of $Zr_2(PO_4)(O_3PCH_2CH_2(viologen)CH_2CH_2PO_3)X_3{\cdot}3H_2O$, (X = halide),[14] $Zr_2(O_3PCH_2CH_2{-}viologen{-}CH_2CH_2PO_3)F_6{\cdot}2H_2O$,[15] $Zr(O_3PCH_2Cl)_2$,[16] etc.[17–20] cannot be determined through single-crystal X-ray diffraction (SCXRD) due to their poor crystallinity, and structural models obtained from powder X-ray diffraction (PXRD) data may exhibit significant deviation. Highly crystalline zirconium phosphonates are extremely rare.[3,5,7,8,21–25] Therefore, a key scientific challenge in developing zirconium phosphonate materials is devising strategies to enhance their crystallinity.

[a]College of Chemistry, Fuzhou University, Fuzhou 350116, Fujian, China
[b]State Key Laboratory of Structural Chemistry, Fujian Institute of Research on the Structure of Matter, Chinese Academy of Sciences, Fuzhou, Fujian 350002, China. E-mail: shy@fjirsm.ac.cn, fml@fjirsm.ac.cn
[c]Fujian College, University of Chinese Academy of Sciences, Fuzhou, 350002, P.R. China
[d]College of Chemistry and Materials Science, Fujian Normal University, Fuzhou 350007, P. R. China
[e]University of Chinese Academy of Sciences, Beijing, 100049, P. R. China

Open Access Article. Published on 07 November 2025. Downloaded on 1/31/2026 4:42:54 PM.
This article is licensed under a Creative Commons Attribution-NonCommercial 3.0 Unported Licence.

In order to improve the crystallinity of Zr-MOFs, researchers have developed various strategies. An effective one is to incorporate competitive ligands (*e.g.*, acetic acid and benzoic acid[26]) to regulate the coordination environment of ZrO_6 clusters and thus decrease the nucleation rate. For instance, the effect of benzoic acid or acetic acid concentration on the crystallinity of Zr-bdc (UiO-66) has been investigated by adjusting ligand dosages. The results show that with increasing regulator concentration, the product morphology transitioned from interwoven crystals to individual crystals.[27] Another strategy is to introduce fluorides to enable the formation of strong Zr–F bonds, thereby significantly enhancing the crystallinity and thermal stability of Zr-MOFs.[28] For example, Noro *et al.* reported the solvothermal synthesis of fluorinated MOFs, in which zirconium atoms coordinate with fluorine atoms to form a framework structure.[29] It was found that the presence of fluorine atoms enhanced the crystallinity and thermal stability of Zr-MOFs. Therefore, it is expected that under the action of hydrogen fluoride (HF), Zr can coordinate with organic phosphate ligands to obtain the zirconium fluorophosphonates with high crystallinity and stability. However, currently, zirconium fluorophosphonates synthesized in the presence of hydrofluoric acid remain scarce.[11,30–35] The reported zirconium fluorophosphonates SZ-1 ($[C_4mpyr][Zr_{2.5}(TppmH_3)F_6]\cdot 2.5H_2O$), C_4mpyr = *N*-butyl-*N*-methylpyrrolidinium, $TppmH_8$ = (tetrakis[4-(dihydroxyphosphoryl)phenyl]methane) and SZ-3 ($[C_2py]_2[Zr_{3.5}(TppaH)F_9]\cdot 6.5H_2O$, C_2py = *N*-ethylpyridinium, TppaH = 1,3,5,7-tetrakis(4-phosphonophenyl)adamantine)[11] exhibit high stability in aqua regia and possess ion exchange properties towards various ions. Moreover, the highly crystalline zirconium fluorophosphonates facilitate the study on the correlation of the structure and property, as exemplified by SZ-8 ($K_2Zr[CH_2(PO_3)_2]F_2$),[31] SZ-7 ($[(CH_3)_2NH_2]_2[ZrC_6H_4(CH_2PO_3)_2F_2]$)[33] and SZ-4 ($[(CH_3)_2NH_2][ZrCH_2(PO_3)_2F]$),[34] which clearly demonstrate that the selectivity of their ion exchange performance is primarily due to the affinity between functional groups within the structures and target ions. On the other hand, due to the discriminative nature, the highest electronegativity, and low polarizability of the F atom, it can form strong hydrogen bonds.[36] As a result, unique properties, such as proton conduction and gas adsorption, have been developed in F-containing molecules/materials.[37] Notably, despite these advantages, zirconium fluorophosphonates with proton conduction properties are limited. Thus far, only two zirconium fluorophosphonates $(DMA)_3[Zr(HL)F_2]$[38] (H_6L = 2,4,6-tris(4-phosphonophenyl) pyridine, DMA^+ = dimethylammonium) and $ZrF[H_3(O_3PCH_2NHCH_2COO)_2]$[35] with proton conduction performance have been reported. Thus, the development of highly crystalline zirconium fluorophosphonates for proton conduction remains a critical research priority.

In this work, two two-dimensional (2D) fluorophosphonate Zr-MOFs, $A_2[Zr(hedp)F_2]$ ($hedpH_2$ = 1-hydroxyethylidene-1,1-diphosphonic acid, $A^+ = K^+$ (**1**), NH_4^+ (**2**)), were synthesized in HF media and with *N*,*N*-dimethylacetamide as the solvent. Their structures feature the anionic layer of $[Zr(hedp)F_2]_n^{2n-}$ with A^+ cations located in interlayer spaces. Compounds **1** and **2** exhibit proton conduction performance, attributed to their abundant –OH, F, and $-PO_3$ groups, which form the dense hydrogen-bonding networks. Notably, compound **2** exhibits better proton conductivity due to the presence of NH_4^+ cations, which facilitate the extensive hydrogen bonding network. This structural feature enables more efficient proton transport pathways compared with that of compound **1**. The mechanism of the proton conduction is clarified as well. Notably, the compounds retain the structural stability after proton conduction. By introducing HF as the structure-directing agent, this study successfully prepared highly crystalline fluorophosphonate Zr-MOFs. This work overcomes the long-standing challenge of low crystallinity in zirconium fluorophosphonates, yielding new zirconium fluorophosphonates, and demonstrates their potential as proton-conducting materials.

Materials and methods

Materials

Hydroxyethylidenediphosphonic acid (96.00%, Shanghai Titan Technology Co., Ltd), $ZrOCl_2\cdot 8H_2O$ (98.00%, Shanghai Adamas Reagent Co., Ltd), HF (AR, ≥40 nt Co., Ltd), *N*,*N*-dimethylacetamide (99.00%, Sinopharm Chemical Reagent Co., Ltd), HNO_3 (AR, Sinopharm Chemical Reagent Co., Ltd), KNO_3 (99.90%, Greagent Reagent Co., Ltd), terephthalic acid (AR, Fuchen Chemical Reagent Co., Ltd), and NH_4OH (AR, Sinopharm Chemical Reagent Co., Ltd) were used. All commercial reagents were used without additional purification.

Syntheses of 1

The synthesis of compound **1** was achieved under solvothermal conditions. In a typical procedure, $ZrOCl_2\cdot 8H_2O$ (257.8 mg, 0.8 mmol), $hedpH_2$ (164.8 mg, 0.8 mmol), KNO_3 (262.9 mg, 2.6 mmol), 8 mL *N*,*N*-dimethylacetamide, 2 mL deionized water, and 0.08 mL HF were mixed in a 28 mL stainless steel autoclave with a Teflon liner. The pH of the system was titrated to 3 using 0.28 mL HNO_3. After vigorously stirring for 30 minutes at room temperature, the sealed reactor was heated at 180 °C for 3 days and then allowed to naturally cool to laboratory temperature. The resulting crystalline product was collected by filtration, washed thoroughly with deionized water and ethanol (three times each), and dried under ambient conditions (yield: 0.217 g, 61% based on Zr atoms). Elemental analysis: calcd, C: 5.87%, H: 0.99%, N: 0.00%. Found, C: 5.66%, H: 0.97%, N: 0.00%.

Synthesis of 2

Compound **2** was synthesized through a modified solvothermal approach. Using a 28 mL Teflon-lined stainless-steel autoclave, we combined 0.8 mmol $ZrOCl_2\cdot 8H_2O$ (257.8 mg, 0.8 mmol), $hedpH_2$ (164.8 mg, 0.8 mmol), terephthalic acid (83.1 mg, 0.5 mmol), 1 mL ammonium hydroxide (NH_4OH), 8 mL *N*,*N*-dimethylacetamide, 2 mL deionized water, and 0.08 mL HF. The reaction mixture was carefully adjusted to a

 This journal is © The Royal Society of Chemistry 2025

Open Access Article. Published on 07 November 2025. Downloaded on 1/31/2026 4:42:54 PM.
This article is licensed under a Creative Commons Attribution-NonCommercial 3.0 Unported Licence.

pH of 3 with 0.78 mL HNO_3. After homogenizing the mixture by stirring for 30 minutes at room temperature, the sealed reactor was heated to 180 °C and held for 72 hours under autogenous pressure before being slowly cooled to ambient temperature. The resulting crystalline product was isolated by filtration, subjected to three successive washing cycles with deionized water and ethanol, and finally air-dried to obtain crystals for compound **2** (yield: 0.197 g, 67% based on Zr atoms). Elemental analysis: calcd, C: 6.54%, H: 3.29%, N: 7.62%. Found, C: 6.62%, H: 2.99%, N: 7.74%.

Proton conduction experiments

Compounds **1** and **2** were separately ground into homogeneous microcrystalline powders and then pressed into cylindrical pellets with a radius of 0.126 cm using a tablet press. Silver paste was uniformly coated on both the top and bottom surfaces of the pellets to serve as electrodes, which were then connected with gold wires to ensure good electrical contact. During the preparation process, special attention was paid to maintaining consistent sample thickness and preventing short circuits along the sidewalls. First, tests were conducted at a constant temperature of 25 °C under relative humidity levels of 65%, 75%, 85%, and 95%. When the humidity reaches 95%, the temperature is adjusted to 35 °C, 45 °C, 55 °C, 65 °C, 75 °C and 85 °C sequentially for further testing. Each time the humidity was set, we waited for 2 hours before testing and collecting data. Each time the temperature was adjusted, we waited for 1 hour before testing and collecting data.

Characterization techniques

PXRD patterns were recorded at RT by using a Miniflex II diffractometer with CuK_α radiation (λ = 1.54178 Å) in a 2θ range of 5–65°. Thermogravimetric analysis (TG) was conducted using a Netzsch STA449C thermoanalyzer instrument from 20 °C to 1200 °C at a heating rate of 10 °C min^{-1} under a N_2 atmosphere. Nonmetallic elements such as C, H, and N in the samples were quantitatively analyzed with the Vario EL Cube element analyzer (EA, Elementar, Germany). The proton conduction test was performed on an SI 1260 IMPEDANCE/GAINPHASE impedance analyzer. The temperature and humidity control during the proton conduction test was carried out in the Haotianxin constant temperature and humidity test chamber (model SMA-100PF). The water vapor adsorption experiments were conducted using the gas adsorption detector BETSORP instrument. The surface morphology of the compounds was determined through 165 scans using a scanning electron microscope (SEM, model JSM-6700F from JEOL). The applied voltage used in the test is 50 mV, and the frequency range is 0.1 Hz–1 MHz. Energy-dispersive X-ray spectroscopy (EDX) was performed using a JSM-6700F scanning electron microscope (JEOL, Showa, Japan) and SU-8010 field emission scanning electron microscope (HITACHI, Japan). The Fourier-transform infrared (FTIR) spectra were recorded in the 400–4000 cm^{-1} range by using ATR on a Bruker VERTEX 70 FTIR spectrophotometer. Crystals of appropriate size and dimensions were selected and placed under a microscope and then the crystals were fixed at the tip of a glass fiber for SCXRD characterization. SCXRD data of **1** were collected on a Rigaku XtaLAB-Synergy-R diffractometer at 100 K using MoK_α (λ = 0.71073 Å) and SCXRD data of **2** were collected on a Rigaku XtaLAB-Synergy-R diffractometer at 298 K using CuK_α (λ = 1.54178 Å). The structures were solved by direct methods and refined by full-matrix least-squares on F^2 using the SHELX-2019 program package.[39]

Results and discussion

Crystal structures

The crystal structures were unambiguously determined through SCXRD analysis (Table S1). EA, TG (Fig. S1), FTIR (Fig. S2) and EDX (Fig. S3) together verified the correctness of the empirical formulas. The anionic frameworks of A_2[Zr(hedp)F_2] ($A^+ = K^+$ (**1**), NH_4^+ (**2**)) are the same, but their cations are different. Therefore, using compound **1** as a representative example, the structures of title compounds are described. Its asymmetric unit contains one Zr atom, one hedp ligand, two F atoms, and two K^+ cations (Fig. 1a). Each Zr atom coordinates with four oxygen atoms of four $-PO_3$ groups from three hedp ligands. That is, the Zr atom is coordinated with one hedp ligand through double-dentate chelation and connected with the other two hedp ligands through monodentate coordination. In addition, the Zr atom also coordinates with two F atoms, finally forming an octahedral ZrO_4F_2 coordination geometry (Fig. 1b). Owing to an hedp ligand being connected to the same Zr, a slight distortion of the ZrO_4F_2 octahedron occurs. The bond lengths of Zr–F are 1.9999(14) and 2.0081(14) Å, and those of Zr–O are in the range of 2.0564(17)–2.0951

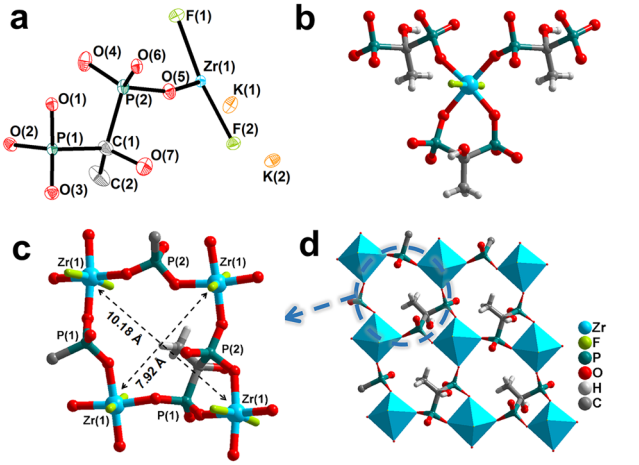

Fig. 1 (a) ORTEP plot (50% ellipsoid probability) showing the crystallographic asymmetric unit of compound **1**. Hydrogen atoms are omitted for clarity. (b) Octahedral coordination of Zr in compound **1** represented in the ball-and-stick mode. (c) Ball-and-stick representation of the eight-membered ring in the anionic layer of **1**. (d) An anionic layer in compound **1**.

Open Access Article. Published on 07 November 2025. Downloaded on 1/31/2026 4:42:54 PM.
This article is licensed under a Creative Commons Attribution-NonCommercial 3.0 Unported Licence.

(16) Å. The bond angle range of ∠F–Zr–O is 86.03(6)–94.87(6)°, and the bond angle range of ∠O–Zr–O is 83.75(7)–172.39(7)° (Table S2). Four ZrO_4F_2, a complete ligand, and two $-PO_3$ groups come into being in the eight-membered rings, in which the spacing between Zr atoms is 10.18 × 7.92 $Å^2$ (Fig. 1c). Through sharing Zr–O–P–O–Zr edges and ZrO_4F_2 corners, these windows extend infinitely, forming a $[Zr(hedp)F_2]_n^{2n-}$ layer (Fig. 1d). Here, O(4)···H(7A) represents the shortest distance between the two layers, with a value of 2.16 Å (Fig. S4). The layers are stacked in the direction of the *c*-axis with a horizontal shift (Fig. 2a), and K^+ ions balance the anion charges in each layer. The layers are connected by hydrogen bonds, where the H(7A) atom in –OH of hedp forms a hydrogen bond with the unpaired O(4) atom in $-PO_3$, and the –F(1) forms a hydrogen bond with the H(3B) atom in $-CH_3$ of hedp (Table S3). From a perspective view along the *c*-axis, the hydrogen bonds form wavy hydrogen bond channels in between the two layers (Fig. 2b).

In compound **2** (Tables S4 and S5), the eight-membered ring size is 10.26 × 7.92 $Å^2$ (Fig. S5). The interlayer O(4)···H(7) distance is found to be 2.85 Å (Fig. S6). The NH_4^+ ions reside in the interlayer spaces and balance the charges of anionic layers. From the perspective views of the *b*-axis (Fig. 2c) and *a*-axis (Fig. 2d), there are numerous hydrogen bonds among the networks.

PXRD

The experimental PXRD patterns of compound **1** (Fig. 3a) and compound **2** (Fig. 3b) show no additional peaks when compared with the simulated PXRD patterns derived from their respective SCXRD data. This indicates that the experimentally obtained samples are of the same phase as the structurally characterized single crystals, confirming that compounds **1** and **2** can be synthesized as pure phases.

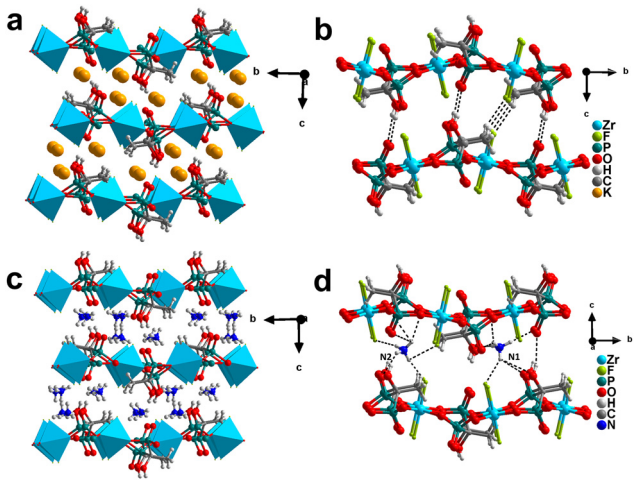

Fig. 2 (a) Packing diagram of compound **1** viewed along the *a*-axis. (b) The interlayer hydrogen bonds in compound **1**. (c) Packing diagram of compound **2** viewed along the *a*-axis. (d) The interlayer hydrogen bonds in compound **2**.

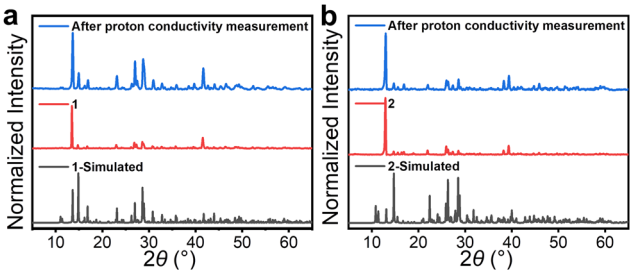

Fig. 3 (a) Comparison of PXRD patterns for compound **1** before and after proton conductivity testing with the simulated pattern from the single-crystal X-ray structure. (b) Comparison of PXRD patterns for compound **2** before and after proton conductivity testing with the simulated pattern from the single-crystal X-ray structure.

Water adsorption

Water vapor adsorption experiments of compounds **1** and **2** show that at 25 °C and a P/P_0 of 0.98 compound **1** adsorbed 3.61 mg g^{-1} of water vapor, while compound **2** adsorbed 11.66 mg g^{-1} of water vapor. This indicates that compounds **1** and **2** possess significant hydrophilic properties, which is attributed to the abundance of hydrophilic groups ($-PO_3$ and –OH) in both structures (Fig. S7). Therefore, proton conduction of compounds **1** and **2** may occur using water as the medium.

Proton conduction

Proton conduction materials exhibit significant application potential in hydrogen sensors and proton exchange membrane fuel cells.[40] Generally, non-coordination functional groups in the organic ligands of MOFs (*e.g.*, –OH and $-PO_3H_2$) facilitate efficient proton conduction.[41] In addition, the hydrogen bond networks in the structure may enhance proton transfer. The $-PO_3$, –OH, and –F groups in compounds **1** and **2**, and the presence of NH_4^+ in compound **2** contribute to the more abundant hydrogen bonds. These structural features prompt us to investigate their proton conduction by alternating current impedance spectroscopy. The proton conductivity was investigated *via* impedance spectra. The samples after proton conductivity testing were subjected to PXRD analysis. A comparison of the PXRD patterns revealed no additional peaks in the patterns before and after proton conduction, indicating that the framework of compounds **1** and **2** remained structurally intact after the conductivity test (Fig. 3a and b).

At 25 °C, the proton conductivities (σ) of **1** and **2** were measured under varying relative humidity (65%–95% RH) (Fig. S8a, S8b, and Table S6). The σ increased from 1.61 × 10^{-7} S cm^{-1} to 3.96 × 10^{-5} S cm^{-1} for **1** and 1.41 × 10^{-6} S cm^{-1} to 5.88 × 10^{-4} S cm^{-1} for **2** when the RH ranged from 65% to 95%. These results indicate that the increase of relative humidity enhances the adsorption of the material to water and produces more proton carriers, thus enhancing the proton conductivity.

Temperature is another critical factor for proton conductivity. Thus, proton conductivity was subsequently measured

 This journal is © The Royal Society of Chemistry 2025

Open Access Article. Published on 07 November 2025. Downloaded on 1/31/2026 4:42:54 PM.
This article is licensed under a Creative Commons Attribution-NonCommercial 3.0 Unported Licence.

under different humidity conditions (95% RH) over a temperature gradient from 35 to 85 °C. According to the Nyquist plots (Fig. 4a, and Table S7), when the temperature rises from 45 °C to 85 °C, the proton conductivities could increase from 3.67 × 10^{-4} to 6.37 × 10^{-4} S cm^{-1} for **1**, and when the temperature changes from 35 °C to 85 °C (Fig. 4b, and Table S7), the proton conductivities could increase from 3.11 × 10^{-3} to 1.27 × 10^{-2} S cm^{-1} for **2**. Elevated temperatures facilitate water adsorption by the materials, thereby promoting the formation of proton carriers and enhancing proton conductivity.[42]

As can be seen from Table S8, compound **2** has higher proton conductivity than those of most other phosphonate based compounds, such as $[Cd_2(L^1)_2(Bib)_2(H_2O)]\cdot 4.5H_2O$ (L^1 = 4-carboxyphenylmethylphosphonate ethyl ester), $[Cd(L^2)(Bib)]\cdot 3H_2O$ (L^2 = 3-carboxyphenylmethylphosphonate ethyl ester), Bib = 1,4-bis-(1*H*-imidazol-1-yl)benzene,[43] $[Tb(H_2L)(H_2bts)(H_2O)]\cdot H_2O$ (H_3bts = 5-sulfoisophthalic acid, H_4L = bis-methylenephosphonic acid),[44] PGM-L3 and PGMH1,[45] and is second only to those of Na-MOF (1.03 × 10^{-1} S cm^{-1} at 60 °C and 98% RH)[46] and PCMOF20 (1.3 × 10^{-2} at 85 °C and 95% RH).[38]

The proton conduction mechanisms of compounds **1** and **2** were further investigated. As shown in Fig. 4c and d, the linear relationship between ln(σT) and 1000/T is observed upon fitting based on the Arrhenius equation. The calculated activation energy values for compounds **1** and **2** are 0.124 eV and 0.310 eV, respectively, which are below 0.4 eV, indicating that proton conduction proceeds *via* a hopping mechanism. The experimental results of water adsorption, TG (Fig. S1), and SEM (Fig. S9) demonstrate the involvement of water in the proton conduction process. The proton conduction of title compounds proceeds *via* water-mediated proton transfer and follows the Grotthuss mechanism.[40,47]

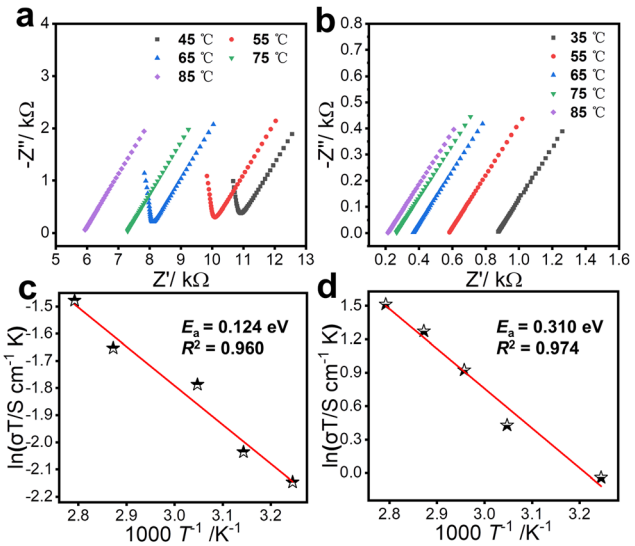

Fig. 4 Nyquist plots of **1** (a) and **2** (b) as a function of temperature at 95% relative humidity. The Arrhenius plots of **1** (c) and **2** (d) as a function of temperature under 95% RH.

Structural analysis reveals that the 2D anionic $[Zr(hedp)F_2]_n^{2n-}$ layers of both compounds feature –OH and –F groups oriented perpendicular to the interlayer regions, participating in hydrogen bonding to form continuous proton conduction pathways (Tables S3 and S5, Fig. 2b and d).[48] Compound **2** contains NH_4^+ cations that form N–H···O and N–H···F hydrogen bonds with the framework, creating strong hydrogen-bonded chains along the *b*-axis (Table S5). Protons are transported efficiently along these chains *via* a hopping mechanism.[49] Although water-mediated proton conduction represents a common mechanism in many materials, the introduction of NH_4^+ can significantly enhance the proton transport efficiency.[50] For instance, after introducing NH_4^+ into the KZn_6-HPAA-3D structure, its proton conductivity increases by two orders of magnitude.[40,51] Therefore, although compounds **1** and **2** are isomorphic, the difference in their cationic components leads to distinct hydrogen-bonding networks. These structural variations ultimately account for their different proton conductivities.

Conclusions

This work reports the successful synthesis of two isostructural highly crystalline zirconium fluorophosphonates $\{A_2[Zr(hedp)F_2]\}$ (A^+ = K^+ (**1**), NH_4^+ (**2**)) *via* the solvothermal method with HF addition. The anionic $[Zr(hedp)F_2]_n^{2n-}$ layers are integrated with the A^+ cations occupying the interlayer spaces of title structures. Under the conditions of 95% RH and 85 °C, compounds **1** and **2** show proton conduction behavior with a σ of 6.37 × 10^{-4} S cm^{-1} and 1.27 × 10^{-2} S cm^{-1}, consistent with the Grotthuss mechanism. The proton conductivity is primarily ascribed to the abundant hydrogen bonds around the framework functional groups such as F, –OH and $-PO_3$ which serve as the primary pathways for proton migration. Comparative analysis reveals that compound **2**, incorporating NH_4^+ cations, demonstrates significantly enhanced proton conductivity relative to compound **1**. This study not only expands the family of crystalline zirconium fluorophosphonates but also validates that constructing hydrogen-bonding networks within the structure is a viable strategy to enhance the proton conductivity.

Author contributions

S. Z. Liu: data curation, writing – reviewing and editing, validation, formal analysis, investigation, and software. Y. Y. Zhao: data curation, writing original draft and formal analysis. Y. W. Ren: formal analysis. Z. Y. Chen: validation and review. L. Yang: project administration and resources. Z. H. Chen: resources and visualization. H. Y. Sun: funding acquisition, supervision, reviewing and editing. Z. X. Wei: resources. M. L. Feng: conceptualization, writing – reviewing and editing, funding acquisition, resources, visualization, supervision, and project administration. X. Y. Huang: reviewing and editing, conceptualization, resources, visualization, supervision, and project administration.

Open Access Article. Published on 07 November 2025. Downloaded on 1/31/2026 4:42:54 PM.
This article is licensed under a Creative Commons Attribution-NonCommercial 3.0 Unported Licence.

Conflicts of interest

There are no conflicts to declare.

Data availability

The original contributions presented in this study are included in the article/supplementary information (SI). Further inquiries can be directed to the corresponding author.

Supplementary information: proton conductivity measurement and additional tables (Tables S1–S8) and figures (Fig. S1–S9). See DOI: https://doi.org/10.1039/d5dt01846c.

CCDC 2466567 and 2466570 contain the supplementary crystallographic data for this paper.[52a,b]

Acknowledgements

This research was funded by the National Natural Science Foundation of China (No. 22325605, U21A20296, and 22406185), the Natural Science Foundation of Fujian Province (No. 2024J08105) and the Strategic Priority Research Program of the Chinese Academy of Sciences (No. XDB1170000).

References

1 J. Zhang, S. Yao, S. Liu, B. Liu, X. Sun, B. Zheng, G. Li, Y. Li, Q. Huo and Y. Liu, *Cryst. Growth Des.*, 2017, **17**, 2131–2139.
2 F. Zhou, B. Zheng, D. Liu, Z. Wang and Q. Yang, *ACS Appl. Mater. Interfaces*, 2019, **11**, 46984–46992.
3 A. Donnadio, M. Nocchetti, F. Costantino, M. Taddei, M. Casciola, F. da Silva Lisboa and R. Vivani, *Inorg. Chem.*, 2014, **53**, 13220–13226.
4 L. Shi, Z. Yang, F. Sha and Z. Chen, *Sci. China: Chem.*, 2023, **66**, 3383–3397.
5 T. Rhauderwiek, H. Zhao, P. Hirschle, M. Döblinger, B. Bueken, H. Reinsch, D. De Vos, S. Wuttke, U. Kolb and N. Stock, *Chem. Sci.*, 2018, **9**, 5467–5478.
6 R. R. Liang, Y. Yang, Z. Han, V. I. Bakhmutov, J. Rushlow, Y. Fu, K. Y. Wang and H. C. Zhou, *Adv. Mater.*, 2024, **36**, 202407194.
7 M. Nocchetti, A. Donnadio, E. Vischini, T. Posati, C. Albonetti, D. Campoccia, C. R. Arciola, S. Ravaioli, V. Mariani, L. Montanaro and R. Vivani, *Inorg. Chem.*, 2022, **61**, 2251–2264.
8 G. H. Chen, Y. P. He, S. H. Zhang and L. Zhang, *Inorg. Chem. Commun.*, 2018, **97**, 125–128.
9 Q. He, J. Shen, X. Guan, Y. Han, X. Jiang, X. Shen, X. Huang, Y. Chen, C. Lei, X. Xiao and W. Lin, *Anorg. Allg. Chem.*, 2021, **648**, e202100248.
10 D. Feng, Z. Y. Gu, Y. P. Chen, J. Park, Z. Wei, Y. Sun, M. Bosch, S. Yuan and H. C. Zhou, *J. Am. Chem. Soc.*, 2014, **136**, 17714–17717.
11 T. Zheng, Z. Yang, D. Gui, Z. Liu, X. Wang, X. Dai, S. Liu, L. Zhang, Y. Gao, L. Chen, D. Sheng, Y. Wang, J. Diwu, J. Wang, R. Zhou, Z. Chai, T. E. A. Schmitt and S. Wang, *Chem. Commun.*, 2017, **8**(1), 15369.
12 H. H. Liu, J. Pan, Z. Z. Xue, S. D. Han, J. H. Li and G. M. Wang, *Cryst. Growth Des.*, 2019, **19**, 5326–5333.
13 G. K. H. Shimizu, R. Vaidhyanathan and J. M. Taylor, *Chem. Soc. Rev.*, 2009, **38**, 1430–1449.
14 H. Byrd, A. Clearfield, D. Poojary, K. P. Reis and M. E. Thompson, *Chem. Mater.*, 1996, **8**, 2239.
15 D. M. Poojary, L. A. Vermeulen, E. Vicenzi, A. Clearfield and M. E. Thompson, *Chem. Mater.*, 1994, **6**, 1845–1849.
16 D. M. Poojary, C. Bhardwaj and A. Clearfield, *J. Mater. Chem.*, 1995, **5**, 171–174.
17 A. Donnadio, M. Pica, M. Taddei and R. Vivani, *J. Mater. Chem.*, 2012, **22**, 5098.
18 M. Taddei, F. Costantino and R. Vivani, *Inorg. Chem.*, 2010, **49**, 9664–9670.
19 M. N. U. Costantino and R. Vivanid, *J. Am. Chem. Soc.*, 2002, **124**, 8428–8434.
20 P. H. Mutin, D. Medoukali and A. Vioux, *J. Mater. Chem.*, 1999, **9**, 2553–2557.
21 F. Costantino, A. Donnadio and M. Casciola, *Inorg. Chem.*, 2012, **51**, 6992–7000.
22 C. Y. Gao, J. Ai, H. R. Tian, D. Wu and Z. M. Sun, *Chem. Commun.*, 2017, **53**, 1293–1296.
23 R. Vivani, F. Costantino, U. Costantino and M. Nocchetti, *Inorg. Chem.*, 2006, **45**, 2388–2390.
24 M. Taddei, S. J. I. Shearan, A. Donnadio, M. Casciola, R. Vivani and F. Costantino, *Dalton Trans.*, 2020, **49**, 3662–3666.
25 J. Zhang, L. Chen, D. Gui, H. Zhang, D. Zhang, W. Liu, G. Huang, J. Diwu, Z. Chai and S. Wang, *Dalton Trans.*, 2018, **47**, 5161–5165.
26 D. Feng, H. L. Jiang, Y. P. Chen, Z. Y. Gu, Z. Wei and H. C. Zhou, *Inorg. Chem.*, 2013, **52**, 12661–12667.
27 A. Schaate, P. Roy, A. Godt, J. Lippke, F. Waltz, M. Wiebcke and P. Behrens, *Chem. – Eur. J.*, 2011, **17**, 6643–6651.
28 N. Prasetyo and F. I. Pambudi, *Int. J. Hydrogen Energy*, 2021, **46**, 4222–4228.
29 S. Noro and T. Nakamura, *NPG Asia Mater.*, 2017, **9**, e433.
30 F. Costantino, P. Sassi, M. Geppi and M. Taddei, *Cryst. Growth Des.*, 2012, **12**, 5462–5470.
31 J. R. Zhang, L. Chen, L. H. Chen, L. Chen, Y. G. Zhang, C. L. Chen, Z. F. Chai and S. A. Wang, *Dalton Trans.*, 2022, **51**, 14842–14846.
32 B. Zhang, D. M. Poojary and A. Clearfield, *Inorg. Chem.*, 1998, **37**, 249–254.
33 J. R. Zhang, L. Chen, X. Dai, L. X. Chen, F. W. Zhai, W. F. Yu, S. K. Guo, L. J. Yang, L. H. Chen, Y. G. Zhang, L. W. He, C. L. Chen, Z. F. Chai and S. A. Wang, *Chem. Commun.*, 2021, **57**, 8452–8455.
34 J. R. Zhang, L. H. Chen, X. Dai, L. Zhu, C. L. Xiao, L. Xu, Z. Y. Zhang, E. V. Alekseev, Y. X. Wang, C. Zhang, H. W. Zhang, Y. L. Wang, J. Diwu, Z. F. Chai and S. A. Wang, *Chem*, 2019, **5**, 977–994.

 This journal is © The Royal Society of Chemistry 2025

Open Access Article. Published on 07 November 2025. Downloaded on 1/31/2026 4:42:54 PM.
This article is licensed under a Creative Commons Attribution-NonCommercial 3.0 Unported Licence.

35 M. Taddei, A. Donnadio, F. Costantino, R. Vivani and M. Casciola, *Inorg. Chem.*, 2013, **52**, 12131–12139.
36 Z. H. Guo, Q. Yu, Y. C. Chen, J. Liu, T. Li, Y. H. Peng and W. H. Yi, *Chem. Rec.*, 2023, **23**, e202300108.
37 W. Zhang, J. Zhang, X. T. Dong, M. L. Li, Q. He, S. Zhao and L. X. Xie, *Chem. Eng. J.*, 2023, **461**, 142058.
38 Z. H. Fard, N. E. Wong, C. D. Malliakas, P. Ramaswamy, J. M. Taylor, K. Otsubo and G. K. H. Shimizu, *Chem. Mater.*, 2018, **30**, 314–318.
39 G. M. Sheldrick, *Acta Crystallogr., Sect. C:Struct. Chem.*, 2015, **71**, 3–8.
40 P. Ramaswamy, N. E. Wong and G. K. H. Shimizu, *Chem. Soc. Rev.*, 2014, **43**, 5913–5932.
41 S. S. Bao, G. K. H. Shimizu and L. M. Zheng, *Coord. Chem. Rev.*, 2019, **378**, 577–594.
42 T. Y. Pan, W. Y. Wen, W. Ma, S. T. Zheng, M. L. Feng and X. Y. Huang, *Dalton Trans.*, 2024, **53**, 2318–2323.
43 Y. N. Zhou, D. Y. Liu, J. H. Yu, X. Li, C. Y. Huang, H. W. Zheng, C. Q. Jiao, Y. Y. Zhu and Z. G. Sun, *J. Mol. Struct.*, 2025, **1329**, 141418.
44 Y. N. Zhou, L. L. Liu, Q. W. Liu, X. X. Liu, M. Z. Feng, L. Wang, Z. G. Sun, Y. Y. Zhu, X. Zhang and C. Q. Jiao, *Inorg. Chem.*, 2021, **60**, 17303–17314.
45 N. Mukherjee, O. Basu, S. Mukhopadhyay and T. Jana, *ACS Appl. Polym. Mater.*, 2024, **6**, 7488–7499.
46 X. T. Bai, L. H. Cao, X. Y. Chen, X. J. Cao, W. C. Meng and K. Y. Yan, *Cryst. Growth Des.*, 2023, **23**, 8488–8493.
47 G. Alberti and M. Casciola, *Solid State Ionics*, 2001, **145**, 3–16.
48 P. Rought, C. Marsh, S. Pili, I. P. Silverwood, V. G. Sakai, M. Li, M. S. Brown, S. P. Argent, I. V. Yrezabal, G. Whitehead, M. R. Warren, S. Yang and M. Schröder, *Chem. Sci.*, 2019, **10**, 1492–1499.
49 Y. S. Wei, X. P. Hu, Z. Han, X. Y. Dong, S. Q. Zang and T. C. W. Mak, *J. Am. Chem. Soc.*, 2017, **139**, 3505–3512.
50 S. Chai, R. L. Zhong, Y. L. Zhu, H. Guo, X. Li, S. He, Y. Zhu and H. Li, *Nano Lett.*, 2025, **25**, 9741–9747.
51 R. M. P. Colodrero, I. R. Salcedo, M. B. García, D. F. M. Pérez, J. D. D. Martín, E. R. Losilla, L. M. Real, J. Rius, M. A. G. Aranda, K. D. Demadis, P. O. Pastor and A. Cabeza, *Pure Appl. Chem.*, 2017, **89**, 75–87.
52 (*a*) CCDC 2466567: Experimental Crystal Structure Determination, 2025, DOI: 10.5517/ccdc.csd.cc2nsnpt; (*b*) CCDC 2466570: Experimental Crystal Structure Determination, 2025, DOI: 10.5517/ccdc.csd.cc2nsnsx.